Journal of Computational Physics **155,** 307–330 (1999)
Article ID jcph.1999.6334, available online at http://www.idealibrary.com on IDEAL®

An Accurate Curved Boundary Treatment in the Lattice Boltzmann Method

Renwei Mei,* Li-Shi Luo,† and Wei Shyy*

*Department of Aerospace Engineering, Mechanics and Engineering Science, University of Florida, Gainesville, Florida 32611-6250; †ICASE, NASA Langley Research Center, Hampton, Virginia 23681-2199
E-mail: rwm@aero.ufl.edu, luo@icase.edu, wei-shyy@ufl.edu

Received February 2, 1999; revised June 29, 1999

The lattice Boltzmann equation (LBE) is an alternative kinetic method capable of solving hydrodynamics for various systems. Major advantages of the method are due to the fact that the solution for the particle distribution functions is explicit, easy to implement, and natural to parallelize. Because the method often uses uniform regular Cartesian lattices in space, curved boundaries are often approximated by a series of stairs that leads to reduction in computational accuracy. In this work, a second-order accurate treatment of the boundary condition in the LBE method is developed for a curved boundary. The proposed treatment of the curved boundaries is an improvement of a scheme due to O. Filippova and D. Hänel (1998, *J. Comput. Phys.* **147**, 219). The proposed treatment for curved boundaries is tested against several flow problems: 2-D channel flows with constant and oscillating pressure gradients for which analytic solutions are known, flow due to an impulsively started wall, lid-driven square cavity flow, and uniform flow over a column of circular cylinders. The second-order accuracy is observed with a solid boundary arbitrarily placed between lattice nodes. The proposed boundary condition has well-behaved stability characteristics when the relaxation time is close to $1/2$, the zero limit of viscosity. The improvement can make a substantial contribution toward simulating practical fluid flow problems using the lattice Boltzmann method. © 1999 Academic Press

I. INTRODUCTION

There has been a rapid progress in developing and employing the method of the lattice Boltzmann equation (LBE) [1–3] as an alternative computational technique for solving complex fluid dynamic problems (see the comprehensive reviews in [4, 5]). In a traditional method for computational fluid dynamics (CFD), the macroscopic variables, such as velocity $\boldsymbol{u}$ and pressure p, are obtained by solving the Navier–Stokes (NS) equations [6–8]. The lattice Boltzmann equation approximates the kinetic equation for the particle mass

0021-9991/99 $30.00
Copyright © 1999 by Academic Press
All rights of reproduction in any form reserved.

distribution function $f(\boldsymbol{x}, \boldsymbol{\xi}, t)$ on the mesoscopic level, such as the Boltzmann equation with the single relaxation time approximation [9],

$$\frac{\partial f}{\partial t} + \boldsymbol{\xi} \cdot \nabla f = -\frac{1}{\lambda}\left(f - f^{(0)}\right), \tag{1}$$

where $\boldsymbol{\xi}$ is the particle velocity, $f^{(0)}$ is the equilibrium distribution function (the Maxwell–Boltzmann distribution function), and λ is the relaxation time. The right hand side (RHS) term models the effect of the fluid viscosity on the molecular level through the collision (relaxation) process. The macroscopic quantities (such as mass density ρ and momentum density $\rho\boldsymbol{u}$) are the hydrodynamic moments of the distribution function f,

$$\rho = \int f(\boldsymbol{x}, \boldsymbol{\xi}, t)\, d^3\boldsymbol{\xi} \tag{2a}$$

$$\rho\boldsymbol{u} = \int \boldsymbol{\xi} f(\boldsymbol{x}, \boldsymbol{\xi}, t)\, d^3\boldsymbol{\xi}. \tag{2b}$$

It has been shown that the velocity space $\boldsymbol{\xi}$ can be discretized into a finite set of points $\{\boldsymbol{\xi}_\alpha\}$ without affecting the conservation laws [10–12]. In the discretized velocity space the Boltzmann equation (1) becomes

$$\frac{\partial f_\alpha}{\partial t} + \boldsymbol{\xi}_\alpha \cdot \nabla f_\alpha = -\frac{1}{\lambda}\left(f_\alpha - f_\alpha^{(eq)}\right) \qquad (\alpha = 0, 1, 2, \ldots, 8 \text{ for 2-D}) \tag{3}$$

for the distribution function of discrete velocities $f_\alpha(\boldsymbol{x}, t) \equiv f(\boldsymbol{x}, \boldsymbol{\xi}_\alpha, t)$. The equilibrium distribution function, $f_\alpha^{(eq)}$, and the discrete velocity set $\{\boldsymbol{\xi}_\alpha\}$ can be derived explicitly [10–12].

For the 2-D square lattice shown in Fig. 1, we use $\boldsymbol{e}_\alpha$ to denote the discrete velocity set, and we have [13]

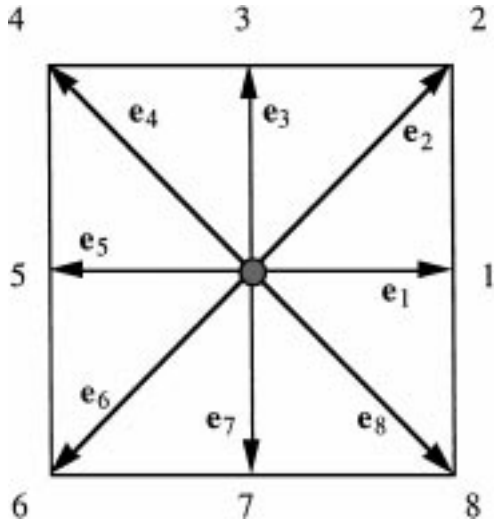

FIG. 1. A 2-D, 9-bit (or 9-velocity) lattice.

$$\begin{aligned} \boldsymbol{e}_\alpha &= 0, \qquad \text{for } \alpha = 0, \\ \boldsymbol{e}_\alpha &= (\cos((\alpha-1)\pi/4), \sin((\alpha-1)\pi/4)) \qquad \text{for } \alpha = 1, 3, 5, 7, \\ \boldsymbol{e}_\alpha &= \sqrt{2}(\cos((\alpha-1)\pi/4), \sin((\alpha-1)\pi/4)) \qquad \text{for } \alpha = 2, 4, 6, 8, \end{aligned} \tag{4}$$

where $c = \delta x/\delta t$, δx, and δt are the lattice constant and the time step size, respectively, and

$$f_\alpha^{(eq)} = \rho w_\alpha \left[1 + \frac{3}{c^2}\boldsymbol{e}_\alpha \cdot \boldsymbol{u} + \frac{9}{2c^4}(\boldsymbol{e}_\alpha \cdot \boldsymbol{u})^2 - \frac{3}{2c^2}\boldsymbol{u}\cdot\boldsymbol{u}\right], \tag{5}$$

where

$$w_\alpha = \begin{cases} 4/9, & \alpha = 0 \\ 1/9, & \alpha = 1, 3, 5, 7 \\ 1/36, & \alpha = 2, 4, 6, 8. \end{cases} \tag{6}$$

With the discretized velocity space, the hydrodynamic moments are given by

$$\rho = \sum_{\alpha=0}^{8} f_\alpha = \sum_{\alpha=0}^{8} f_\alpha^{(eq)} \tag{7a}$$

and

$$\rho \boldsymbol{u} = \sum_{\alpha=1}^{8} \boldsymbol{e}_\alpha f_\alpha = \sum_{\alpha=1}^{8} \boldsymbol{e}_\alpha f_\alpha^{(eq)}. \tag{7b}$$

The speed of sound of this model is $c_s = c/\sqrt{3}$, and the equation of state is that of an ideal gas,

$$p = \rho c_s^2. \tag{8}$$

Equation (3) is one of numerous ways to model the transport equation of f, Eq. (1).

Based on the Chapman–Enskog analysis, the solution for $f_\alpha(\boldsymbol{x}, t)$ may be expanded in the form of

$$f_\alpha(\boldsymbol{x}, t) = f_\alpha^{(eq)}(\boldsymbol{x}, t) + f_\alpha^{(1)}(\boldsymbol{x}, t) + \cdots, \tag{9}$$

where $f_\alpha^{(1)}$ in Eq. (9) is formally smaller than $f_\alpha^{(eq)}$ in the expansion. Substitution of Eq. (9) into Eq. (3) leads to

$$f_\alpha^{(1)}(\boldsymbol{x}, t) = -\lambda \left[\frac{\partial f_\alpha^{(eq)}}{\partial t} + \boldsymbol{e}_\alpha \cdot \nabla f_\alpha^{(eq)}\right]. \tag{10}$$

Proceeding with the Chapman–Enskog analysis, it can be shown that the Euler equations can be recovered from the solution for $f_\alpha^{(eq)}$ and the NS equations are recovered in the near incompressible limit (i.e., the Mach number $M = |\boldsymbol{u}|/c_s \ll 1$) by the first two terms in Eq. (9). The viscosity of the fluid is

$$\nu = \lambda c_s^2. \tag{11}$$

Equation (3) can be further discretized in space and time. The completely discretized form of Eq. (1), with the time step δt and space step $\boldsymbol{e}_\alpha \delta t$, is

$$f_\alpha(\boldsymbol{x}_i + \boldsymbol{e}_\alpha \delta t, t + \delta t) - f_\alpha(\boldsymbol{x}_i, t) = -\frac{1}{\tau}\left[f_\alpha(\boldsymbol{x}_i, t) - f_\alpha^{(eq)}(\boldsymbol{x}_i, t)\right], \tag{12}$$

where $\tau = \lambda/\delta t$, and $\boldsymbol{x}_i$ is a point in the discretized physical space. The above equation is the lattice Boltzmann equation [1–3] with Bhatnagar–Gross–Krook (BGK) approximation [9]. The left-hand side (LHS) of Eq. (12) is physically a streaming process for particles while the RHS models the collisions through relaxation.

Although the lattice Boltzmann equation historically originates from the lattice gas cellular automata [14, 15], it is indeed a special finite difference form of the continuous Boltzmann kinetic equation, i.e., the LHS of Eq. (3) is discretized along the direction of the characteristic line with discretization of phase space and time tied together [10, 11]. The leading order truncation error of such a discretization is then taken into account exactly by modifying the viscosity in the NS equation derived from Eq. (12) to

$$\nu = \left(\tau - \frac{1}{2}\right) c_s^2 \delta t. \tag{13}$$

The positivity of the viscosity thus requires that $\tau > 1/2$. The lattice Boltzmann scheme consists of two computational steps,

$$\text{collision step} \qquad \tilde{f}_\alpha(\boldsymbol{x}_i, \mathrm{t}) - f_\alpha(\boldsymbol{x}_i, \mathrm{t}) = -\frac{1}{\tau}\left[f_\alpha(\boldsymbol{x}_i, \mathrm{t}) - f_\alpha^{(eq)}(\boldsymbol{x}_i, \mathrm{t})\right] \tag{14a}$$

$$\text{streaming step} \qquad f_\alpha(\boldsymbol{x}_i + \boldsymbol{e}_\alpha \delta t, t + \delta t) = \tilde{f}_\alpha(\boldsymbol{x}_i, t), \tag{14b}$$

where f_α and $\tilde{f}_\alpha$ denote the pre- and post-collision state of the distribution function, respectively. The advantages of solving the lattice Boltzmann equation over the NS equations can now be seen. In the kinetic equation for f_α given by Eq. (3), the advection operator is linear in the phase space whereas the convection term is nonlinear in the NS equation. In traditional CFD methods, the pressure is typically obtained by solving the Poisson or Poisson-like equation derived from the incompressible NS equations that can be time consuming. In the LBE method, the pressure is obtained through an extremely simple equation of state $p = \rho c_s^2$. This is an appealing feature of the LBE method. The discretized Eq. (14) for f_α is explicit in form, easy to implement, and natural to parallelize. The collision step is completely local. The streaming step takes very little computational effort at every time step.

However, unlike solving the NS equations for which the non-slip condition for $\boldsymbol{u}$ on a solid wall is satisfied at the macroscopic level, there is no corresponding, physically based boundary condition for f_α on a solid wall at the mesoscopic level. For a lattice node located on the fluid side at $\boldsymbol{x}_f$, as illustrated in Fig. 2, Eq. (14b) clearly indicates a need for the information of $\tilde{f}_\alpha$ at $\boldsymbol{x}_b$ on the solid side. Therefore all the effort in the previous treatment of the boundary conditions in the LBE models is mainly focused on the calculation of $\tilde{f}_\alpha$ moving from the wall into the fluid region. In previous works of the LBE, the most often used boundary condition on the wall is the so-called bounce-back scheme [16–18]. In the bounce-back scheme, after a particle distribution f_α streams from a fluid node at $\boldsymbol{x}_f$ to a boundary node at $\boldsymbol{x}_b$ along the direction of $\boldsymbol{e}_\alpha$, the particle distribution f_α scatters back to

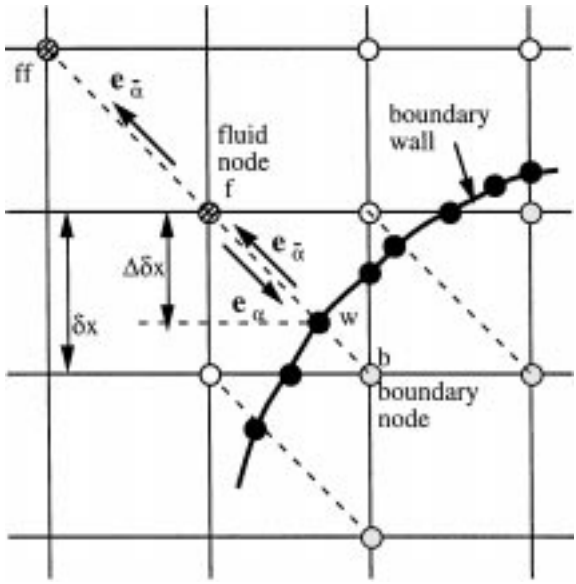

FIG. 2. Layout of the regularly spaced lattices and curved wall boundary.

the node $\boldsymbol{x}_f$ along the direction of $\boldsymbol{e}_{\bar{\alpha}}(=-\boldsymbol{e}_{\alpha})$ as $\tilde{f}_{\alpha}$. Since the wall position $\boldsymbol{x}_w$ was forced to be located at $\boldsymbol{x}_b$, this is referred to as bounce-back on the node (BBN) [19]. However, a finite slip velocity at the stationary wall exists [20, 18] and the accuracy for the flow field is thus degraded due to the inaccuracy of the boundary conditions [17]. In simulating suspension flows using the LBE, Ladd placed the solid walls in the middle between the lattice nodes [21]. This is referred to as bounce-back on the link (BBL). It has been shown that the BBL scheme gives a second-order accurate result for straight walls [24, 18]. Noble *et al.* developed a second-order accurate boundary condition to compute $\tilde{f}_{\alpha}$ but it is only applicable to straight walls in triangular lattice space [22]. He *et al.* generalized the scheme of Noble *et al.* to arbitrary lattice [18]. Chen *et al.* placed the wall on the lattice node so that $\boldsymbol{x}_b$ is one lattice inside the wall [23]. They used an extrapolation of f_{α} on the fluid side (including the wall node) to obtain f_{α} at $\boldsymbol{x}_b$. Zou and He proposed to apply the BBL scheme only for the non-equilibrium part of f_{α} at the wall [24].

For a curved geometry, the use of BBL requires approximation of the curved solid boundary by a series of stair steps. The geometric integrity cannot be preserved by such an approximation. For high Reynolds number flows, the integrity of geometry is important since the vorticity generation and stress distributions are sensitive to the geometrical resolution. To this end, He and Luo proposed to use the LBE with nonuniform grid with second order interpolations [10, 25, 26]. He and Doolen further applied the interpolation to the LBE with curvilinear coordinates or body-fitted coordinates [27]. Mei and Shyy solved Eq. (3) in curvilinear coordinates using the finite difference method [28]. While the wall geometry is accurately preserved in body-fitted coordinates, the flexibility to handle complex geometries is maintained by using the numerical grid generation techniques common to the Navier–Stokes solvers. It should be noted that perhaps the most profound and rigorous theoretical treatment of the boundary condition along the wall is given by Ginzbourg and d'Humières [29]. The scheme proposed by Ginzbourg and d'Humières is local and accurate up to second order in Chapman–Enskog expansion. However, this work has not

attracted sufficient attention because its implementation is not as easy as the bounce-back scheme.

In this work, a robust, second-order accurate treatment for the distribution function f_α near a curved boundary is developed based on the method recently proposed by Filippova and Hänel (hereinafter referred to as FH) [30]. In Ref. [30], the boundary condition for f_α on the solid side is evaluated using Eq. (3) for f_α, and the Taylor series expansion in both space and time for f_α near the wall. FH reported numerical results for a uniform flow over a cylinder [30]. However, it is found in this work that when tested in a pressure driven channel flow (see implementation and discussions in Section II) there is a strong boundary-condition-induced instability when the distance from the wall to the first lattice on the fluid side is less than half of the lattice size.

Using the Taylor series expansion for the velocity $\boldsymbol{u}$ near the wall, a new treatment for f_α near a curved wall is proposed in this work. While maintaining a second-order accuracy of the solution in handling curved walls, the computational stability is improved so that lower viscosity, or higher Reynolds number, can be attained in the LBE simulations. The new boundary condition treatment is tested systematically to assess the temporal and spatial accuracy and robustness in 2-D channel flow with constant and oscillating pressure gradients, flow due to an impulsively started wall, lid-driven square cavity flow, and flow over a column of circular cylinders. Detailed comparisons for the flow field are made with either analytic solutions or well-resolved numerical solutions of the Navier–Stokes equations by using a finite difference method. The improved boundary treatment represents a significant step towards solving practically relevant flow problems using the LBE method.

II. FORMULATION FOR THE IMPROVED BOUNDARY CONDITION

Filippova and Hänel [30] considered a curved boundary lying between the lattice nodes of spacing δx, as illustrated in Fig. 2, and briefly presented the derivation of their scheme for the treatment of a curved boundary. However, they did not offer explanation to justify the theoretical basis of their method. It is instructive to first reexamine their derivation thoroughly. Based on the insight gained, an improved boundary treatment is then proposed.

A. *Reexamination of and Comments on the Filippova–Hänel Treatment*

The macroscopic flow has a characteristic length of L. The lattice nodes on the solid and fluid side are denoted as $\boldsymbol{x}_b$ and $\boldsymbol{x}_f$, respectively, in Fig. 2. The filled small circles on the boundary, $\boldsymbol{x}_w$, denote the intersections of the wall with various lattice links. The boundary velocity at $\boldsymbol{x}_w$, the intersection with the wall on the link between $\boldsymbol{x}_b$ and $\boldsymbol{x}_f$, is $\boldsymbol{u}_w$. The fraction of an intersected link in the fluid region is Δ, that is,

$$\Delta = \frac{|\boldsymbol{x}_f - \boldsymbol{x}_w|}{|\boldsymbol{x}_f - \boldsymbol{x}_b|}. \tag{15}$$

Obviously, $0 \le \Delta \le 1$ and the horizontal or vertical distance between $\boldsymbol{x}_b$ and $\boldsymbol{x}_w$ is $\Delta \cdot \delta x$ on the square lattice. Suppose the particle momentum moving from $\boldsymbol{x}_f$ to $\boldsymbol{x}_b$ is $\boldsymbol{e}_\alpha$ and the reversed one from $\boldsymbol{x}_b$ to $\boldsymbol{x}_f$ is $\boldsymbol{e}_{\bar{\alpha}} = -\boldsymbol{e}_\alpha$. After the collision step, $\tilde{f}_\alpha$ on the fluid side is known, but not on the solid side. (Hereafter we shall use $\boldsymbol{e}_{\bar{\alpha}}$ and $f_{\bar{\alpha}}$ to denote the velocity and the distribution function coming from a solid node to a fluid node, and $f_{\bar{\alpha}}$ is the unknown

to be computed.) To finish the streaming step,

$$f_{\bar{\alpha}}(\boldsymbol{x}_f = \boldsymbol{x}_b + \boldsymbol{e}_{\bar{\alpha}}\delta t, t + \delta t) = \tilde{f}_{\bar{\alpha}}(\boldsymbol{x}_b, t), \tag{16}$$

it is clear that $\tilde{f}_{\bar{\alpha}}(\boldsymbol{x}_b, t)$ is needed. To construct $\tilde{f}_{\bar{\alpha}}(\boldsymbol{x}_b, t)$ based upon some known information in the surrounding, Filippova and Hänel essentially proposed using the linear interpolation [30],

$$\tilde{f}_{\bar{\alpha}}(\boldsymbol{x}_b, t) = (1-\chi)\,\tilde{f}_{\alpha}(\boldsymbol{x}_f, t) + \chi\, f_{\alpha}^{(*)}(\boldsymbol{x}_b, t) + 2w_\alpha \rho \frac{3}{c^2}\boldsymbol{e}_{\bar{\alpha}} \cdot \boldsymbol{u}_w, \tag{17}$$

where $\boldsymbol{u}_w \equiv \boldsymbol{u}(\boldsymbol{x}_w, t)$ is the velocity at the wall and χ is the weighting factor (to be determined) that controls the linear interpolation (or extrapolation) between $\tilde{f}_\alpha(\boldsymbol{x}_f, t)$ and $f_\alpha^*(\boldsymbol{x}_b, t)$, a fictitious equilibrium distribution function given by

$$f_\alpha^{(*)}(\boldsymbol{x}_b, t) = w_\alpha \rho(\boldsymbol{x}_f, t)\left[1 + \frac{3}{c^2}\boldsymbol{e}_\alpha \cdot \boldsymbol{u}_{bf} + \frac{9}{2c^4}(\boldsymbol{e}_\alpha \cdot \boldsymbol{u}_f)^2 - \frac{3}{2c^2}\boldsymbol{u}_f \cdot \boldsymbol{u}_f\right]. \tag{18}$$

In the above, $\boldsymbol{u}_f \equiv \boldsymbol{u}(\boldsymbol{x}_f, \mathrm{t})$ is the fluid velocity near the wall and $\boldsymbol{u}_{bf}$ is to be chosen. It is emphasized here that the weighting factor χ depends on how $\boldsymbol{u}_{bf}$ is chosen. However, the choice of $\boldsymbol{u}_{bf}$ is not unique. For example, either $\boldsymbol{u}_{bf} = \boldsymbol{u}_f$ or a linear extrapolation using $\boldsymbol{u}_{bf} = (\Delta - 1)\boldsymbol{u}_f/\Delta + \boldsymbol{u}_w/\Delta$ appears reasonable.

To determine χ in Eq. (17), FH considered flows under the condition

$$L/(cT) \ll 1, \tag{19}$$

i.e., the flow has an intrinsic characteristic time scale T that is much larger than the advection time on the lattice scale, L/c. This "slow-flow" condition enabled FH to approximate $f_{\bar{\alpha}}(\boldsymbol{x}_f, t + \delta t)$ in Eq. (16) by $f_{\bar{\alpha}}(\boldsymbol{x}_f, t)$,

$$f_{\bar{\alpha}}(\boldsymbol{x}_f = \boldsymbol{x}_b + \boldsymbol{e}_{\bar{\alpha}}\delta t, t + \delta t) = f_{\bar{\alpha}}(\boldsymbol{x}_f, t) + \delta t \frac{\partial f_{\bar{\alpha}}}{\partial t} + \cdots.$$

For the purpose of the order-of-magnitude estimate, it is seen that $O(\partial f_{\bar{\alpha}}/\partial t) = O(f_{\bar{\alpha}}/T)$ so that

$$f_{\bar{\alpha}}(\boldsymbol{x}_f, t+\delta t) = f_{\bar{\alpha}}(\boldsymbol{x}_f, t)\left[1+O\left(\frac{\delta t}{T}\right)\right] = f_{\bar{\alpha}}(\boldsymbol{x}_f, t)\left[1+O\left(\frac{\delta x}{L}\frac{L}{cT}\right)\right] \approx f_{\bar{\alpha}}(\boldsymbol{x}_f, t). \tag{20}$$

It is noted that under condition (19) the neglected terms are of $O(\frac{\delta x}{L}\frac{L}{cT})$ which are much smaller than the $O(\frac{\delta x}{L})$ terms of present interest (in deriving an accurate boundary condition for $\tilde{f}_{\bar{\alpha}}(\boldsymbol{x}_b, t)$). Applying the Chapman–Enskog expansion in the form given by Eqs. (9)–(10) and invoking the "slow flow" approximation, one obtains

$$\begin{aligned} f_{\bar{\alpha}}(\boldsymbol{x}_f, t) &= f_{\bar{\alpha}}^{(eq)}(\boldsymbol{x}_f, t) - \lambda\left[\frac{\partial f_{\bar{\alpha}}^{eq}}{\partial t} + \boldsymbol{e}_{\bar{\alpha}} \cdot \nabla f_{\bar{\alpha}}^{eq}\right] + \cdots \\ &\approx f_{\bar{\alpha}}^{(eq)}(\boldsymbol{x}_f, t) - \lambda \boldsymbol{e}_{\bar{\alpha}} \cdot \nabla f_{\bar{\alpha}}^{eq} + \cdots. \end{aligned} \tag{21}$$

For $f_{\bar{\alpha}}^{(eq)}$ given by Eq. (5), the leading order term in $\nabla f_{\bar{\alpha}}^{eq}$ is given by $\rho w_\alpha (3/c^2)\boldsymbol{e}_{\bar{\alpha}} \cdot \nabla \boldsymbol{u}$ since the rest are higher order terms in the near incompressible flow limit. Noticing that

$\lambda = \tau\delta t$, Eq. (21) becomes

$$f_{\bar{\alpha}}(\boldsymbol{x}_f, t) \approx f_{\bar{\alpha}}^{(eq)}(\boldsymbol{x}_f, t) - \tau\delta t\rho w_\alpha \frac{3}{c^2}\boldsymbol{e}_{\bar{\alpha}} \cdot \nabla\boldsymbol{u} \cdot \boldsymbol{e}_{\bar{\alpha}}$$
$$= f_\alpha^{(eq)}(\boldsymbol{x}_f, t) - 2\rho w_\alpha \frac{3}{c^2}\boldsymbol{u}_f \cdot \boldsymbol{e}_\alpha - \tau\delta t\rho w_\alpha \frac{3}{c^2}\boldsymbol{e}_\alpha \cdot \nabla\boldsymbol{u} \cdot \boldsymbol{e}_\alpha \tag{22}$$

which approximates the LHS of Eq. (16). To expand the RHS of Eq. (16) in terms of the small computational parameter

$$\frac{\delta x}{L} = \frac{c\delta t}{L} \ll 1, \tag{23}$$

it is first noted that $f_\alpha^{(*)}(\boldsymbol{x}_b, t)$ in Eq. (18) can be expressed as

$$f_\alpha^{(*)}(\boldsymbol{x}_b, t) = f_\alpha^{(eq)}(\boldsymbol{x}_f, t) + w_\alpha\rho\frac{3}{c^2}\boldsymbol{e}_\alpha \cdot (\boldsymbol{u}_{bf} - \boldsymbol{u}_f) \tag{24}$$

so that the RHS of Eq. (16), or Eq. (17), can be rewritten as

$$\tilde{f}_{\bar{\alpha}}(\boldsymbol{x}_b, t)$$
$$\approx f_\alpha^{(eq)}(\boldsymbol{x}_f, t) + (1-\chi)(1-1/\tau) f_\alpha^{(1)}(\boldsymbol{x}_f, t) + w_\alpha\rho\frac{3}{c^2}\boldsymbol{e}_\alpha \cdot (\chi\boldsymbol{u}_{bf} - \chi\boldsymbol{u}_f - 2\boldsymbol{u}_w)$$
$$= f_\alpha^{(eq)}(\boldsymbol{x}_f, t) - (1-\chi)(\tau-1)\delta t w_\alpha\rho\frac{3}{c^2}\boldsymbol{e}_\alpha \cdot \nabla\boldsymbol{u} \cdot \boldsymbol{e}_\alpha$$
$$+ w_\alpha\rho\frac{3}{c^2}\boldsymbol{e}_\alpha \cdot (\chi\boldsymbol{u}_{bf} - \chi\boldsymbol{u}_f - 2\boldsymbol{u}_w). \tag{25}$$

Based on linear interpolation, $\boldsymbol{u}_{bf} \approx (\Delta-1)\boldsymbol{u}_f/\Delta + \boldsymbol{u}_w/\Delta$, expanding the velocity $\boldsymbol{u}_f$ near the wall ($\boldsymbol{x}_w$) using Taylor series, and noticing that $\boldsymbol{x}_b - \boldsymbol{x}_f = \delta t\boldsymbol{e}_\alpha$, one obtains $\boldsymbol{u}_{bf} - \boldsymbol{u}_f \approx \delta t\nabla\boldsymbol{u} \cdot \boldsymbol{e}_\alpha$. Equating Eqs. (22) and (25) and matching terms linear in δt results in $\chi = (2\Delta-1)/\tau$. For $\boldsymbol{u}_{bf} = \boldsymbol{u}_f$, we have $\boldsymbol{u}_{bf} - \boldsymbol{u}_f = 0$ in Eq. (25). Matching to $O(\delta t)$ then requires $\chi = (2\Delta-1)/\tau = (2\Delta-1)/(\tau-1)$. FH found that $\boldsymbol{u}_{bf} = (\Delta-1)\boldsymbol{u}_f/\Delta + \boldsymbol{u}_w/\Delta$ gives computationally stable results only for $\Delta > 1/2$. Hence, they proposed that

$$\boldsymbol{u}_{bf} = (\Delta-1)\boldsymbol{u}_f/\Delta + \boldsymbol{u}_w/\Delta \qquad \text{and} \qquad \chi = (2\Delta-1)/\tau \qquad \text{for } \Delta \geq \frac{1}{2} \tag{26}$$

and

$$\boldsymbol{u}_{bf} = \boldsymbol{u}_f \qquad \text{and} \qquad \chi = (2\Delta-1)/(\tau-1) \qquad \text{for } \Delta < \frac{1}{2}. \tag{27}$$

To recapitulate, there are three independent assumptions that have been made in the foregoing derivation. These are: (i) the Chapman–Enskog expansion in the form given by Eqs. (9)–(10) is valid; (ii) the intrinsic time of the unsteady flow must be large compared with the advection time on the lattice scale given by Eq. (19); (iii) the lattice space must be small compared with the characteristic length scale of the flow as given by Eq. (23) so that the Taylor series expansion for the velocity field near the wall is valid. There have been a large number of papers in the existing literature regarding the validity and usefulness of Chapman–Enskog expansion for the solution to the Boltzmann equation. The "slow flow"

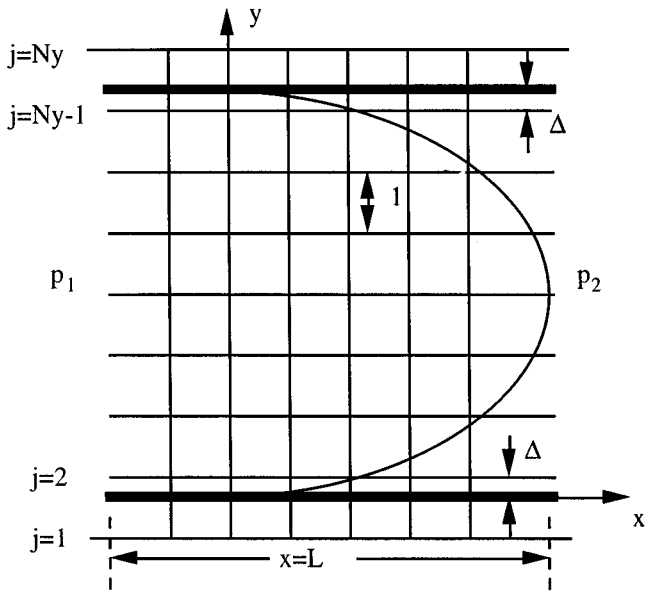

FIG. 3. Lattice distribution in channel flow simulations with arbitrary Δ.

condition is introduced to simplify the derivation of the boundary condition for f_α; the implication of this assumption will be briefly addressed later in comparing the computational results with that based on the conventional bounce-back scheme. The last assumption is a typical computational resolution requirement.

Equation (17) is essentially a linear interpolation (or extrapolation) and is used continuously in the computation. When the weighting factor χ becomes too large, instability may develop. For $\Delta \geq 1/2$, $|\chi| = |2\Delta - 1|/\tau$ is always less than 2 since the positivity of the viscosity in the LBE scheme requires $\tau > 1/2$. For $\Delta < 1/2$, $|\chi| = |(2\Delta - 1)/(\tau - 1)|$ and it may become too large when τ is near 1. To illustrate this point, a fully developed pressure driven 2-D channel flow is considered. The grid arrangement is shown in Fig. 3. For steady flow, a constant pressure gradient ∇p along the x-direction is applied and can be treated as a body force. This is included [32] after the collision step by

$$\tilde{f}_\alpha(\boldsymbol{x}_i, \mathrm{t}) = \tilde{f}_\alpha(\boldsymbol{x}_i, \mathrm{t}) - w_\alpha \frac{3}{c^2}\frac{dp}{dx}\boldsymbol{e}_\alpha \cdot \hat{\boldsymbol{x}}, \tag{28}$$

where $\hat{\boldsymbol{x}}$ is the unit vector along the $\boldsymbol{x}$-axis. The boundary condition for $\tilde{f}_\alpha(\boldsymbol{x}_i, \mathrm{t})$ on the wall follows those given by Eqs. (17), (18), (26), and (27). At the inlet ($i = 1$) and exit ($i = N_x$, in which N_x is the number of lattices in the x-direction) the following is imposed,

$$f_\alpha(i = 1, j) = f_\alpha(i = 2, j), \tag{29}$$

$$f_\alpha(i = N_x, j) = f_\alpha(i = N_x - 1, j). \tag{30}$$

With Eq. (29), the velocity profile at the inlet, $u_x(i = 2, j)$, is not needed. Instead, the fully developed velocity profile is sought as part of the solutions. In this part of the investigation, $N_y = 35$ is used. The exact solution for the velocity profile (given by Eq. (36)) is used as the velocity initial condition which differs from the final steady state solution due to numerical errors. The equilibrium distribution function $f_\alpha^{(eq)}$ based on the exact solution

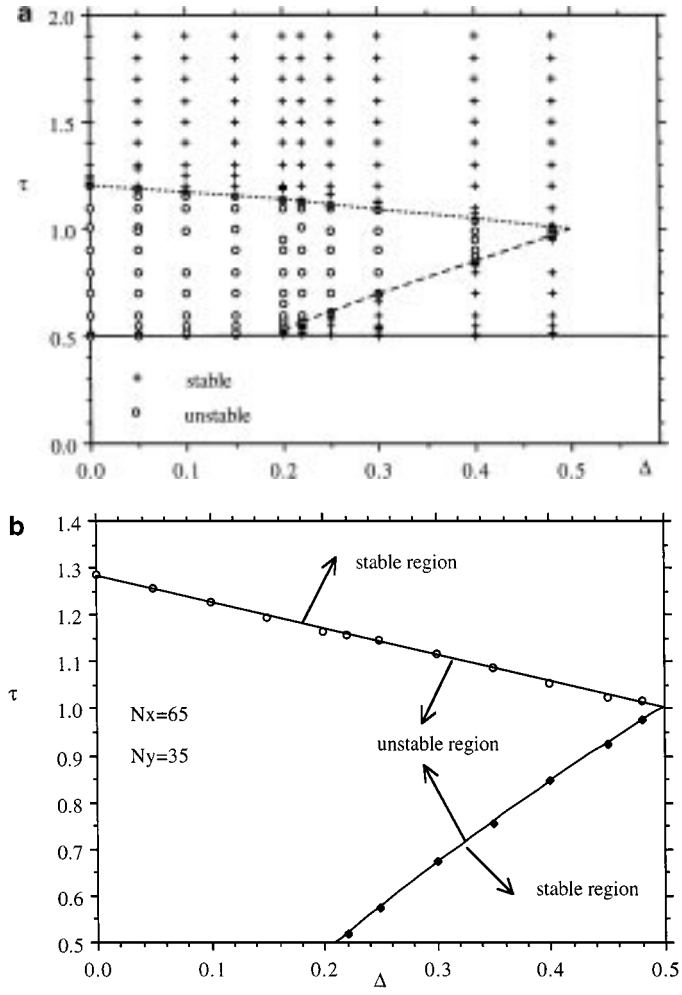

FIG. 4. (a) Regions of stability and instability in the LBE computation for fully developed 2-D channel flow using FH's boundary condition, Eqs. (17), (18), (26), (27), for $\Delta < 1/2$. (b) Regions of stability and instability in the LBE computation for 2-D channel flow entrance problem using FH's boundary condition, Eqs. (17), (18), (26), (27), for $\Delta < 1/2$.

for the velocity profile is used as the initial condition for f_α. The pressure gradient is set to $\frac{dp}{dx} = -1.0 \times 10^{-6}$. All computations are carried out using double precision.

For $\Delta < 1/2$, it is found that the computation is unstable for certain range of values of τ. Figure 4a shows the stability–instability boundaries in the (τ, Δ) space obtained from a large number of computations. For $\Delta < 0.2$, the computation becomes unstable when $\tau < 1$. The large instability region is an apparent source of concern for FH's scheme when $\Delta < 1/2$ since lower viscosity can only be achieved when τ is close to $1/2$.

One may speculate that the instability in the above example results from the lack of specifying an inlet velocity profile, $u_x(y)$, or due to the extrapolation of f_α at the inlet given by Eq. (29). To examine this possibility, a channel flow entrance problem is considered. Uniform velocity profiles, $u_x(y) = -(H^2/12\rho\nu)(dp/dx)$ and $u_y(y) = 0$ in which H is the channel height, are specified at $i = 1.5$ (half-way between the first and second lattices) and the distribution functions $f_\alpha(i = 1, j)$ for $\alpha = 1, 2$, and 8 are obtained using Eq. (17) with

$\chi = 0$ in accordance with $\Delta = 1/2$ at $i = 1.5$. The boundary conditions on the wall are based on Eqs. (17), (18), (26), and (27). The exit boundary condition for the f_α's is given by Eq. (30). Hence the extrapolation for f_α at the inlet is completely eliminated and the velocity profiles at the inlet are exactly given. Two types of initial conditions are used. Whenever possible, the equilibrium distribution functions corresponding to the uniform inlet velocity are specified at $t = 0$ throughout the flow field. This works for relatively larger values of τ. However, instability can be encountered when τ is considerably larger than the upper dash curve shown in Fig. 4a for the same value of Δ ($<1/2$). A second type of initial condition is thus implemented. A converged solution at a relatively large value of τ is used as the initial condition for a smaller value of τ. The value of τ is incrementally decreased to obtain the converged solutions for the new, smaller values of τ. When the actual instability region is approached, the increment in τ is maintained as small as 0.01 or 0.005. In the computation, $\frac{dp}{dx} = -1.0 \times 10^{-6}$, $N_y = 35$, and $N_x = 65$ are used. When the Reynolds number is low (due to the use of the small pressure gradient and larger τ), the exit velocity profile is very close to the exact solution corresponding to the fully developed channel flow which validates the solution procedure.

The stability–instability boundaries obtained through a large number of computations are shown in Fig. 4b. It is noted that the stability–instability boundaries are very similar to that shown in Fig. 4a for the fully developed channel flow despite the dramatic difference in the inlet boundary condition. Thus the source of the instability must result from the implementation of the solid wall condition. An alternative scheme must be developed to overcome this shortcoming.

B. *Improved Treatment for a Curved Boundary*

We realize that the flexibility in the construction of $f_\alpha^{(*)}(\boldsymbol{x}_b, t)$ is the key to achieving an improved computational stability as well as accuracy. Since $\chi = (2\Delta - 1)/(\tau - 1)$ given by Eq. (27) leads to a larger value of χ when τ is close to 1, it is desirable to reduce the magnitude of χ by increasing the magnitude of the denominator in the expression for χ. For $\Delta \geq 1/2$, $\boldsymbol{u}_{bf}$ is the fictitious fluid velocity inside the solid and the denominator for χ is τ. For $\Delta < 1/2$, $\boldsymbol{u}_{bf}$ was chosen by FH to be $\boldsymbol{u}_f$ which is the fluid velocity at $\boldsymbol{x}_f$ and it leads to $(\tau - 1)$ in the denominator for χ. Thus, we propose to use Eq. (26) for $\Delta \geq 1/2$ and use

$$\boldsymbol{u}_{bf} = \boldsymbol{u}_{ff} = \boldsymbol{u}_f(\boldsymbol{x}_f + \boldsymbol{e}_{\bar{\alpha}}\delta t, t) \qquad \text{for } \Delta < \frac{1}{2}. \tag{31}$$

Thus

$$\boldsymbol{u}_{bf} - \boldsymbol{u}_f = \boldsymbol{u}_f(\boldsymbol{x}_f + \boldsymbol{e}_{\bar{\alpha}}\delta t, t) - \boldsymbol{u}_f(\boldsymbol{x}_f, t) = -\delta t \nabla \boldsymbol{u} \cdot \boldsymbol{e}_\alpha. \tag{32}$$

This requires

$$-\tau(1 - \chi)(1 - 1/\tau) - \chi = 2\Delta - \tau \tag{33}$$

to match the $O(\delta t)$ terms in equating Eqs. (22) and (25). Hence

$$\chi = (2\Delta - 1)/(\tau - 2) \qquad \text{for } \Delta < \frac{1}{2}. \tag{34}$$

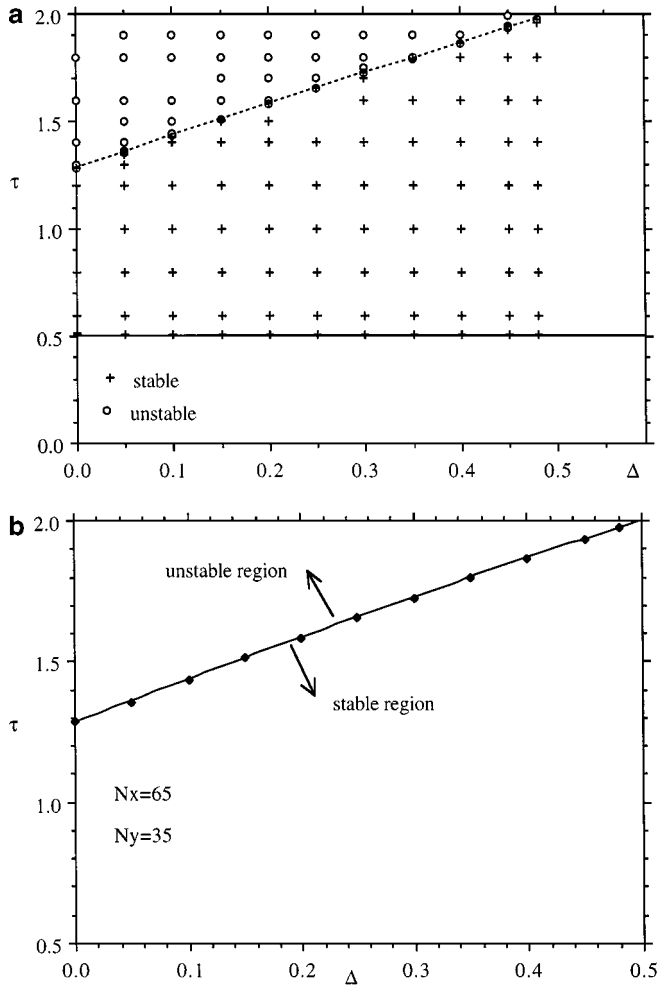

FIG. 5. (a) Regions of stability and instability in the LBE computation for fully developed 2-D channel flow using the present boundary condition, Eqs. (17), (18), (26), (31), (34), for $\Delta < 1/2$. (b) Regions of stability and instability in the LBE computation for the 2-D channel flow entrance problem using the present boundary condition, Eqs. (17), (18), (26), (31), (34), for $\Delta < 1/2$.

To test the improvement in the stability, the steady state, fully developed, pressure driven 2-D channel flow is again considered. Equations (31), (34) are used in lieu of Eq. (27). The rest of the implementation is exactly the same as described in the last section. Figure 5a shows the stability–instability boundary in the (τ, Δ) space for the fully developed channel flow. By comparing Fig. 5a with Fig. 4a, the improvement in the stability of the present treatment for this simple geometry case is clearly seen.

For the channel flow entrance problem, boundary conditions at the inlet and exit and the procedure for specifying the initial conditions are the same as described in the last section. Equations (31), (34) are used to replace Eq. (27) for the solid wall. The stability–instability boundary in the (τ, Δ) space for the entrance flow problem is shown in Fig. 5b. Close agreement in the stability–instability boundaries between Figs. 5a and 5b suggests that the improvement in the computational stability is not related to the treatment of the inlet boundary conditions. The improvement results rather from the different treatment in

the solid wall boundary condition. A direct consequence of this improvement is that lower values of τ, or lower viscosity ν, can now be used.

One may speculate at this point that $\boldsymbol{u}_f(\boldsymbol{x}_f + 2\boldsymbol{e}_{\bar{\alpha}}\delta t, t)$ can also be used for $\boldsymbol{u}_{bf}$ when $\Delta < 1/2$. This would further improve the stability since $\chi = (2\Delta - 1)/(\tau - 3)$. This is correct in principle. However, since the use of $\boldsymbol{u}_f(\boldsymbol{x}_f + \boldsymbol{e}_{\bar{\alpha}}\delta t, t)$ as $\boldsymbol{u}_{bf}$ already allows the use of τ whose value is close to $1/2$, there is little practical need to use $\boldsymbol{u}_f$ that is too far away from the wall.

For transient flows, a second-order extrapolation can be used for

$$\boldsymbol{u}_{bf} = \frac{\Delta - 1}{\Delta}\boldsymbol{u}(\boldsymbol{x}_f, t) + \frac{1}{\Delta}\boldsymbol{u}(\boldsymbol{x}_w, t) + \frac{1 - \Delta}{\Delta(1 + \Delta)}[\boldsymbol{u}(\boldsymbol{x}_w, t) - (1 + \Delta)\boldsymbol{u}(\boldsymbol{x}_f, t) + \Delta\boldsymbol{u}(\boldsymbol{x}_f + \boldsymbol{e}_{\bar{\alpha}}\delta t, t)] \qquad \text{for } \Delta > \frac{1}{2}. \tag{35}$$

This treatment helps to improve the accuracy in the velocity approximation when $\boldsymbol{u}(\boldsymbol{x}, t)$ is not well resolved near the wall. Finally, it is easily seen that the present boundary condition treatment can be extended to 3-D flow problems involving curved geometry. The efficacy of such an extension will be examined in another paper.

III. RESULTS AND DISCUSSIONS

For the proposed boundary condition treatment to be useful, several issues need to be addressed: spatial and temporal accuracy, ability to handle geometric singularity, and the flexibility to handle complex geometry. Channel flows with constant and sinusoidally oscillating pressure gradients with analytic solutions are used to assess the spatial and temporal accuracy. The Stokes first problem (i.e., the flow due to an impulsively started wall) allows one to examine the response of the computed flow field to an imposed singular acceleration. The standard lid-driven cavity flow has a bounded domain but possesses stress or vorticity singularities near the corners between the moving and stationary walls. Finally, flow over a column of circular cylinders is the case used to assess the impact of the boundary treatment on the accuracy of the flow field around a curved boundary.

A. *Pressure Driven Channel Flows*

At steady flow, the exact solution for the $\boldsymbol{x}$-velocity profile is given by

$$u_{exact}(y) = -\frac{1}{2}\frac{dp}{dx}\frac{H^2}{\rho\nu}(\eta^2 - \eta), \tag{36}$$

where $H = N_y - 3 + 2\Delta$ and $\eta = y/H = (j - 2 + \Delta)/H$. To assess the computational error of the LBE solution of the velocity, $u_{LBE}(y)$, the following relative L_2-norm error is defined

$$E_2 = \frac{\left\{\int_0^H [u_{LBE}(y) - u_{exact}(y)]^2\, dy\right\}^{1/2}}{\left[\int_0^H u_{exact}^2(y)\, dy\right]^{1/2}}. \tag{37}$$

With the oscillating pressure gradient, $\frac{dp}{dx} = Be^{-i\omega t}$, the exact solution can be easily expressed in complex variables. An important parameter in this flow is the Stokes number

St defined as

$$St = \sqrt{\frac{H^2\omega}{\nu}}. \tag{38}$$

The Stokes number is the ratio of the channel height H to the thickness of the Stokes layer $\sqrt{\nu/\omega}$. Since the error can vary with time, a time average over one period ($T = 2\pi/\omega$) is needed and the relative error is

$$\mathrm{E}_2 = \frac{\left\{\int_0^T \int_0^H [u_{LBE}(y,t) - u_{exact}(y,t)]^2\, dy\, dt\right\}^{1/2}}{\left[\int_0^T \int_0^H u_{exact}^2(y,t)\, dy\, dt\right]^{1/2}}. \tag{39}$$

In the BGK model, $\Delta t = \Delta x = \Delta y = 1$. Comparing with the channel height $H = N_y - 3 + 2\Delta$, the dimensionless grid size (or grid resolution) is H^1.

Figure 6a shows the dependence of the relative L_2-norm error on the channel height H for $\tau = 0.55$ and $\Delta = 0.0$, 0.25, and 0.5. A maximum value of $N_y = 131$ is used. The second-order accuracy is demonstrated in the range of H investigated. It has been well established that the accuracy of the LBE method for the interior points is of second order. The fact that the overall accuracy is of second order in the present case means that the accuracy in the boundary condition is at least of second order. It is worth noticing that the derivation given in Section II ensures that f_α is second-order accurate near the wall. It does not guarantee the second-order accuracy of the velocity field near the wall. To address this issue, the wall slip velocity, $u_w = u_x(y = 0)$, is evaluated using a second-order extrapolation based on $u_x(y = \Delta)$, $u_x(y = 1 + \Delta)$, and $u_x(y = 2 + \Delta)$. Since the true wall velocity in the pressure driven channel flow is zero, the wall slip velocity u_w provides a measure of the accuracy for the treatment of the wall velocity. Figure 6b shows the dependence of u_w, normalized by the centerline velocity $u_{max} = -(H^2/8\rho\nu)(dp/dx)$, on H for $\Delta = 0.0$, 0.25, and 0.5 with $\tau = 0.55$. Quadratic convergence is clearly observed in all three cases which demonstrates the second-order accuracy of the velocity field near the solid wall. This is entirely consistent with the results shown in Fig. 6a which involves global convergence rather than the local ($y = 0$) convergence. Figure 6c shows the relative error as a function of Δ using the present boundary treatment (Eqs. (17), (18), (26), (31), (34)) for $0 \le \Delta \le 1$. The error in the range of $0 \le \Delta \le 1/2$ is comparable to that in the range of $1/2 < \Delta \le 1$. The present boundary condition treatment does not induce larger computational error and is substantially more robust. Furthermore the second-order accuracy is achieved in general by the present treatment for $\Delta \le 1/2$.

Figure 7 shows the dependence of the relative L_2-norm error on the channel height H in the oscillating pressure driven channel flow for Stokes number $St = H\sqrt{\omega/\nu} = 1$ and 8. For $St = 1$, the Stokes layer is as thick as the channel height H. For $\Delta = 0.25$, 0.5, and 0.75, second-order accuracy in space is clearly demonstrated. Since the time step δt in LBE is equal to the spatial resolution δx, the accuracy in time must also be of second-order in order for the time-averaged L_2-norm error to have a slope of 2 in Fig. 7. For $St = 8$, the Stokes layer thickness is about 1/8 of the channel height so that the computational error due to the insufficient resolution of the Stokes layer is a significant part of the error. For $\Delta = 0.25$, the first lattice in the flow field is only a quarter of the lattice size away from the wall. The Stokes layer is thus better resolved for $\Delta = 0.25$ (denoted by solid circles in Fig. 7) than for $\Delta = 0.5$ and 0.75. However, as H increases, the difference between $\Delta = 0.25$ and $\Delta = 0.5$ and 0.75 becomes smaller since all have reasonable resolutions in the Stokes

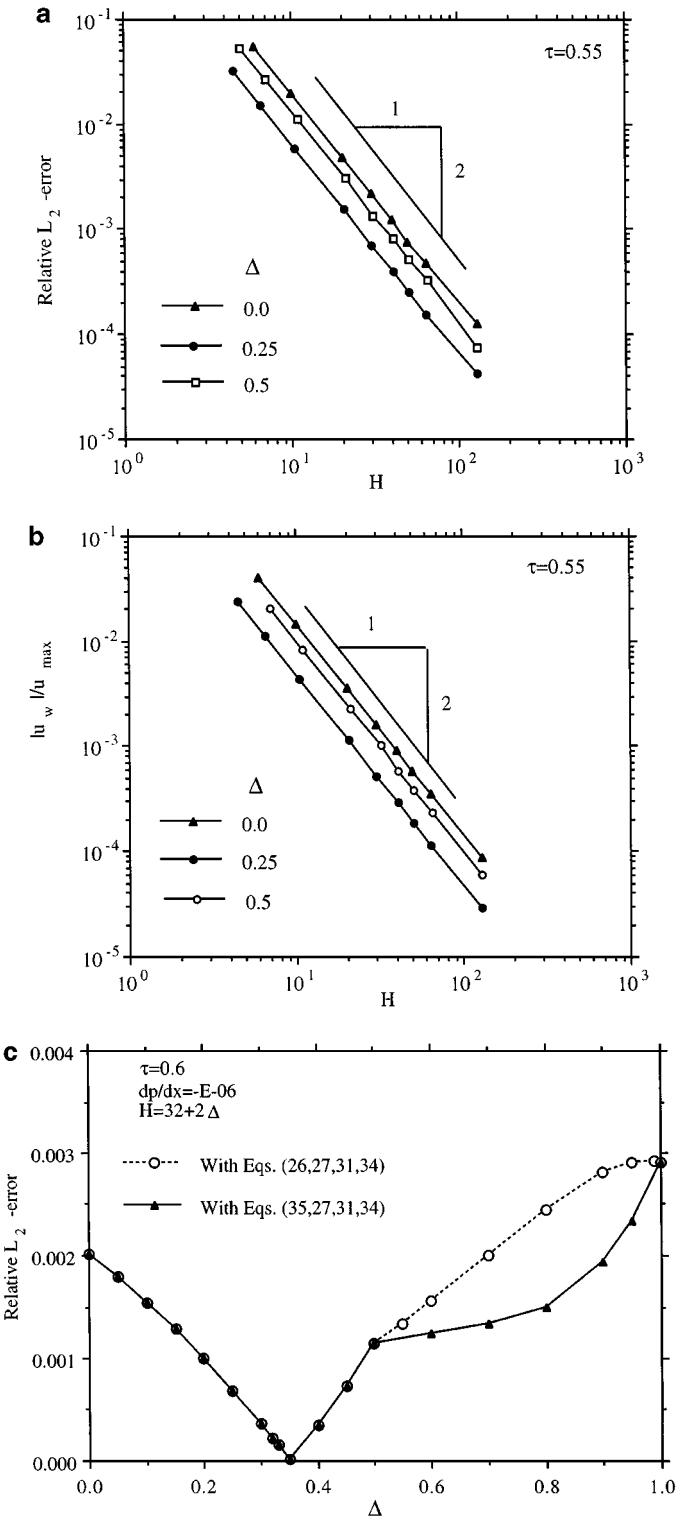

FIG. 6. (a) Dependence of relative L_2-norm error on the lattice resolution $H = N_y - 3 + 2\Delta$, in steady state pressure-driven channel flow simulations. (b) Quadratic convergence of the wall slip velocity in steady state pressure-driven channel flow simulations. (c) Relative L_2-norm error as a function of Δ in steady state pressure-driven channel flow simulations.

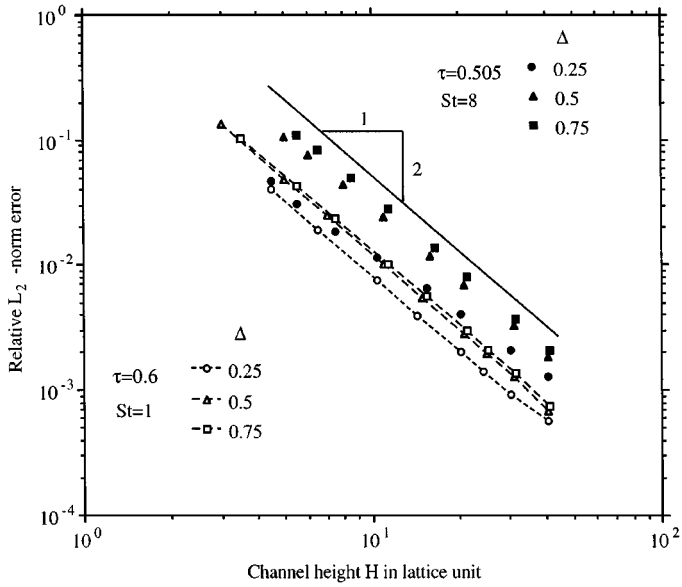

FIG. 7. Dependence of the L_2-norm error on the lattice resolution $H = N_y - 3 + 2\Delta$ in oscillating pressure driven channel flow. Stokes number $St = H\sqrt{\omega/\nu}$.

layer. Although the slope for the error curve for $\Delta = 0.25$ is observed to be about 1.5 that is less than 2, it is an indication of the better-than-expected accuracy at the low resolution end.

B. *Stokes First Problem: Flow Due to an Impulsively Started Wall*

For a wall located at $y = 0$ that is impulsively started, an unsteady Stokes layer of thickness $O(\sqrt{\nu t})$ develops near the wall. For a fixed-grid computation, the error at small time is expected to be large due to insufficient spatial resolution. In the LBE method, this is also compounded by the use of fixed δt $(= \delta x = \delta y = 1)$. Figure 8 shows the velocity profiles at $t = 100$ (in lattice unit). The wall velocity is $V = 0.1$ in lattice unit. The relaxation time $\tau = 0.52$ gives kinematic viscosity $\nu = 0.0067$. Similar to the oscillating pressure driven channel flow, the error is smaller for $\Delta = 0.25$ than for $\Delta = 0.5$ and 0.75 due to a better spatial resolution near the wall. Figure 9 shows the temporal variation of the relative L_2-norm error defined as

$$E_2 = \frac{\left\{\int_0^\infty [u_{LBE}(y,t) - u_{exact}(y,t)]^2\, dy\right\}^{1/2}}{\left[\int_0^\infty u_{exact}^2(y,t)\, dy\right]^{1/2}} \tag{40}$$

for $\Delta = 0.25$, 0.5, and 0.75. The result using the standard *bounce-back on the link* (BBL) scheme, which always sets $\Delta = 0.5$, is also shown. The large relative errors in the beginning are due to the smaller values of the denominator in the above equation. It should be emphasized that this flow at small time is difficult to deal with for any computational technique due to the singular acceleration and large spatial gradient. For an impulsively started Couette flow, the long-time solution approaches the exact linear velocity profile because the LBE method is a second-order accurate one. It is interesting to note that the present boundary

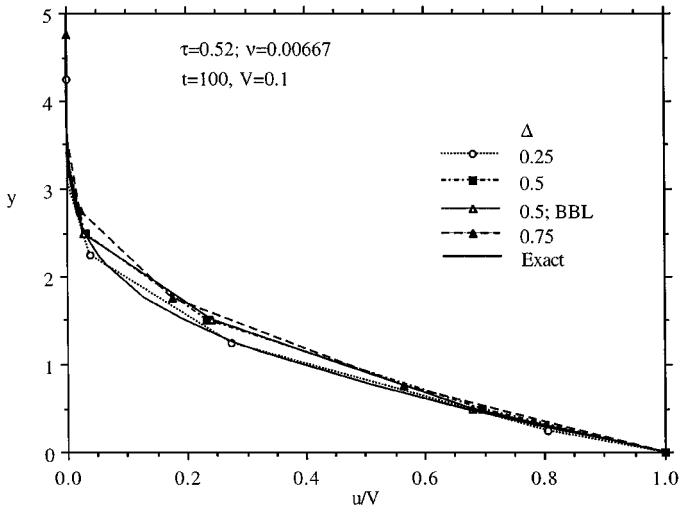

FIG. 8. Velocity profiles at $t = 100$ (lattice unit) of an impulsively started plate with various values of Δ. The bounce back on the link (BBL) always sets $\Delta = 1/2$.

condition treatment for $\Delta = 0.5$ gives a slightly smaller error than the BBL scheme in this highly transient case. In such a transient flow, the computational accuracy in the near-wall region is typically dictated by the near-wall spatial resolution which must be smaller than the Stokes layer thickness in order to resolve the local flow field. In a finite difference calculation for such a flow, δt and δx can be independently chosen. If δx is not sufficiently small, further reduction in δt will not lead to improvement in accuracy. At small t, neither the BBL scheme nor the present treatment resolved the Stokes layer so that the error is large. After the Stokes layer grows to a certain thickness, the spatial resolution becomes adequate

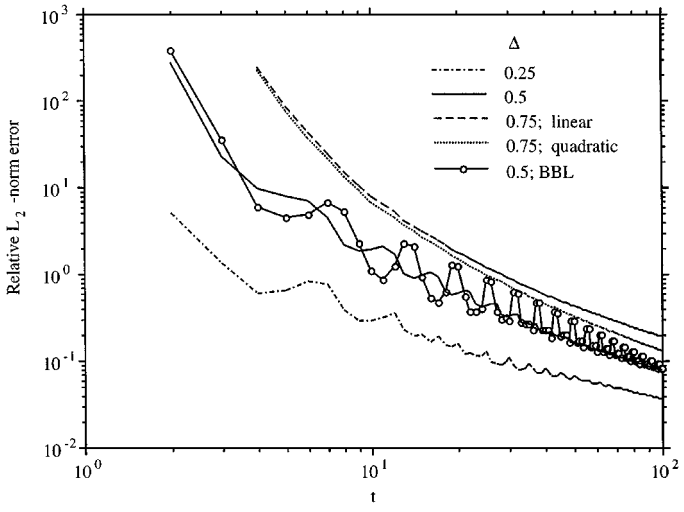

FIG. 9. Relative L_2-norm error of the velocity profile $u_x(y)$ during the initial transient of the impulsively started plate with various values of Δ. The "linear" version of the boundary condition corresponds to Eq. (26). The "quadratic" version corresponds to Eq. (35). The BBL is limited to $\Delta = 0.5$ only.

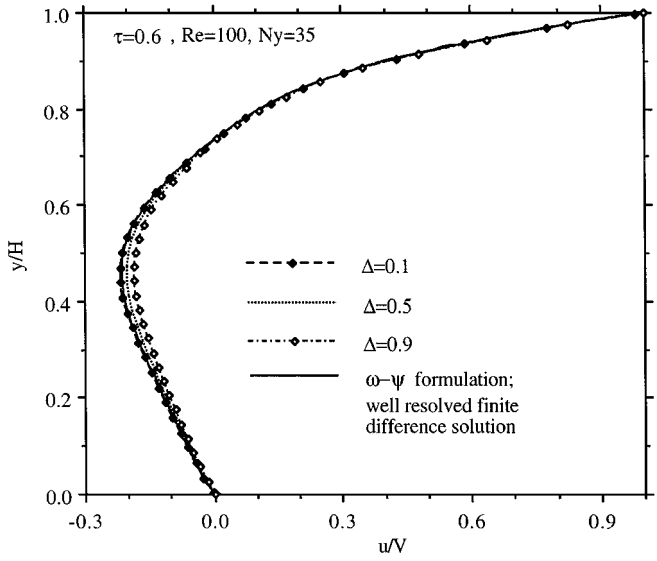

FIG. 10. Velocity profiles at the center $(x/H = 1/2)$ in lid-driven cavity flow with various values of Δ at $\mathrm{Re} = 100$.

and the accuracy then improves. In view of the "slow flow" condition (19) introduced in the derivation, the performance of the current boundary treatment is comparable or better than the conventional bounce-back on the link scheme.

C. *Flow in a Lid-Driven Square Cavity*

Figure 10 shows the velocity profiles at the center $(x/H = 1/2)$ of the cavity of width H at $Re = 100$ with $\tau = 0.6$. Only 35×35 lattices are used and the cavity width is $H = N_x - 3 + 2\Delta = 32 + \Delta$. This requires the lid velocity to be $V = \nu Re/H = 3.33/H$ in the lattice unit. It has a negligible compressibility effect for $H \sim 32$. A well-resolved finite difference solution for the velocity field based on the stream function-vorticity formulation is also shown for comparison. The velocity profile with $\Delta = 0.1$ agrees well with the finite difference solution. For $\Delta = 0.5$, the result is rather reasonable with such a resolution. The difference is slightly larger on the negative velocity part for $\Delta = 0.9$. The corner singularity in stress (or vorticity) is well handled for $\tau = 0.6$ and $N_x = 35$. However, for τ close to 0.5 and with $N_x = 35$, the corner singularity induces wiggles in the velocity field. This issue will be examined elsewhere. The flow field for $Re = 1000$ is obtained with 67×67 lattices using $\Delta = 0.1$, 0.5, and 0.9. Similar behavior in the velocity profiles is observed.

D. *Uniform Flow over a Column of Circular Cylinders*

To simulate the external flow over a single cylinder would require placing the outer boundary far away from the cylinder. In order to keep the computational effort at a reasonable level in using constant space lattices, a column of circular cylinders of radius r and center-to-center distance H is considered instead. The flow field that needs to be computed is thus limited to $-H \le y \le H$. At $y = -H$, the lattice is $j = 2$. The boundary conditions

at $j = 1$ for the f_α's are given by the following symmetry properties,

$$\begin{aligned} f_0(i,1) &= f_0(i,3), & f_1(i,1) &= f_1(i,3), & f_2(i,1) &= f_8(i,3), \\ f_3(i,1) &= f_7(i,3), & f_4(i,1) &= f_6(i,3), & f_5(i,1) &= f_5(i,3), \\ f_6(i,1) &= f_4(i,3), & f_7(i,1) &= f_3(i,3), & f_8(i,1) &= f_2(i,3). \end{aligned} \tag{41}$$

Similar conditions hold at $y = H$ for $j = N_y$. At the inlet, the uniform velocity, $u = V$, is specified at $i = 1.5$. Using $\Delta = 0.5$, $\chi = 0$, Eq. (17) is applied to obtain the f_α's at $i = 1$. At the exit, a simple extrapolation is used,

$$f_\alpha(N_x, j) = 2 f_\alpha(N_x - 1, j) - f_\alpha(N_x - 2, j) \qquad \text{for } \alpha = 4, 5, \text{ and } 6. \tag{42}$$

On the surface of the circular cylinder, Eqs. (17), (18), (26), (31), and (34) proposed in this paper are used to update the boundary conditions for the f_α's.

Figure 11 shows the velocity profile $u(x = 0, y)/V$ for $H/r = 20$ at $Re = 2Vr/\nu = 10$ using $r = 3.5$. Two values of relaxation time τ (=0.505 and 0.525) are used. For $r = 3.5$, there are only 7 lattices from the front to the back stagnation points. The finite difference solution is obtained using body-fitted coordinates [33] and over 200 grid points are distributed along the upper surface of the circle. These two solution with $\tau = 0.505$ and $\tau = 0.525$ are virtually identical to each other and they are both close to the finite difference solution. Figure 12 shows the centerline ($y = 0$) velocity variations, upstream and downstream, respectively, at $Re = 10$ and 40. The sharp gradient near the front stagnation point, the length of the separation bubble, the maximum of the separation bubble velocity, and the recovery of the wake velocity are all in excellent agreement with the well resolved finite difference solution.

As can be seen now, an important improvement of the present boundary condition treatment over the bounce-back scheme is that it can preserve the accuracy of the geometry

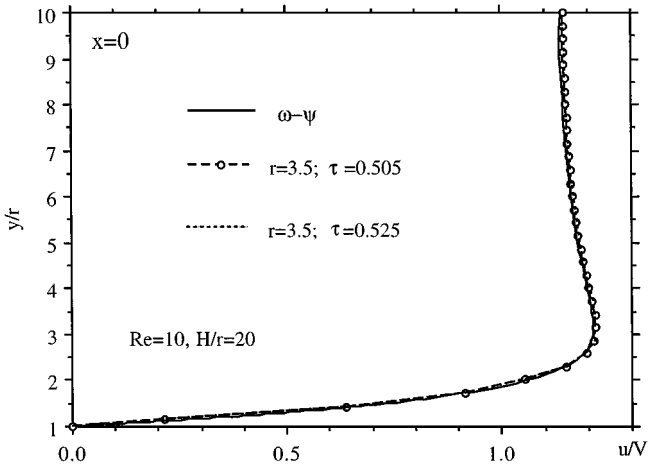

FIG. 11. Velocity profiles at $x = 0$ for uniform flow over a column of cylinders. The cylinder has a diameter ($2r$) of 7 lattice units. The cylinder center-to-center distance $H = 70$ lattice units.

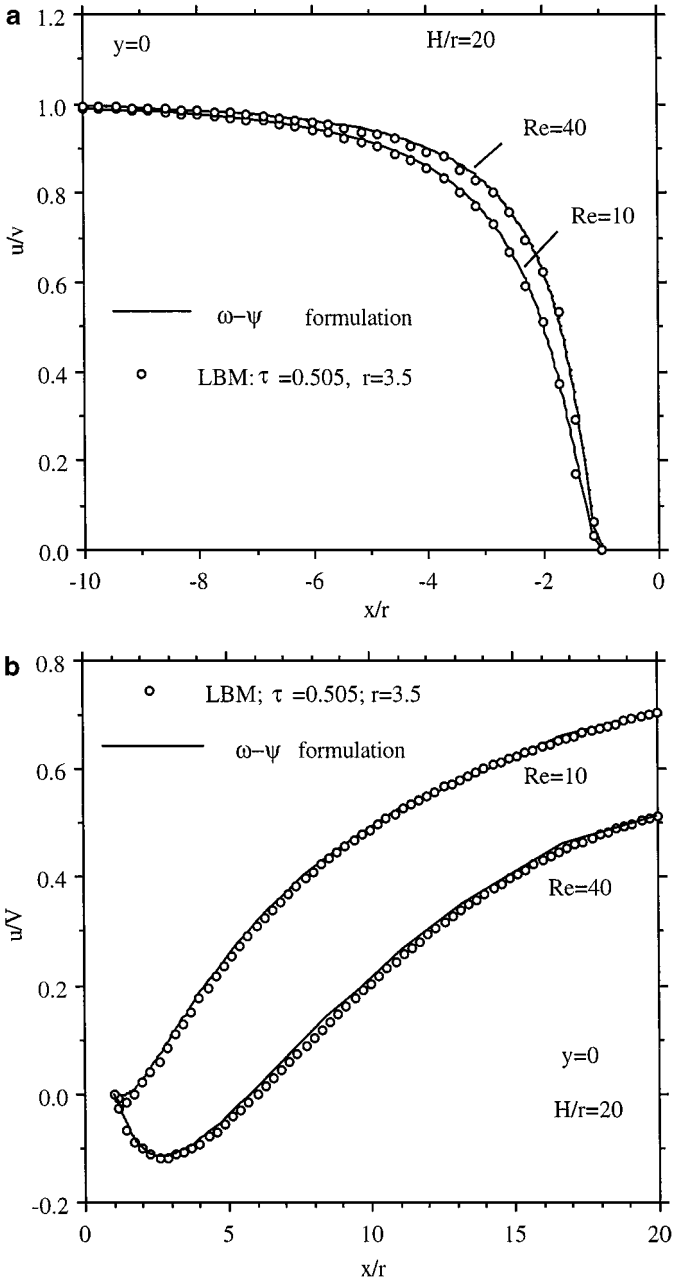

FIG. 12. Centerline ($y = 0$) velocity variation for a uniform flow over a column of cylinders. Finite difference results are based on $\omega - \psi$ formulation and are well resolved. (a) Upstream; (b) downstream.

under consideration. To further demonstrate this point, consider flow over a circular cylinder of radius (r) with the coordinate centered at the center of the cylinder. For $r = 3.4$ and 3.8, the front stagnation points are located at $x = -3.4$ and 3.8, respectively. With the bounce-back on the link (BBL) scheme, the front stagnation points in both cases will be placed at $x = -3.5$ which is half-way between the lattice at $x = -4$ and $x = -3$ on the centerline. In the present method, $\Delta = 0.6$ and 0.2 for r = 3.4 and 3.8, respectively. The

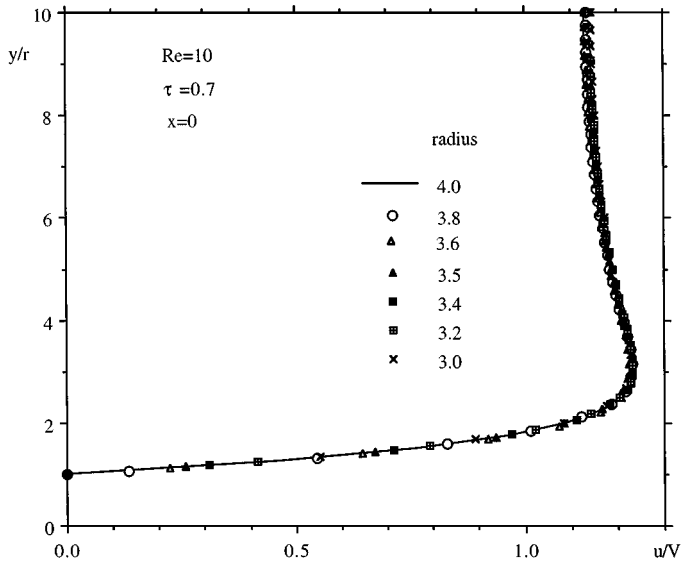

FIG. 13. Comparison of the velocity profiles at $x = 0$ for $r = 3.0$, 3.2, 3.4, 3.5, 3.6, 3.8, and 4.0 for $\mathrm{Re} = 10$ and $H/r = 20$.

difference in Δ can be accurately incorporated in the evaluation of $\tilde{f}_{\bar{\alpha}}(\boldsymbol{x}_b, t)$. This implies that although the boundary links for $r = 3.4$ will be different from those for $r = 3.8$, the flow fields based on $r = 3.4$ and $r = 3.8$ should be nearly the same when the coordinates are normalized by the radius r. To validate this point, a series of computations are carried out for $r = 3.0$, 3.2, 3.4, 3.5, 3.6, 3.8, and 4.0 for $H/r = 20$ at $Re = 10$. The profiles of the dimensionless x-component velocity u_x/U as a function of y/r at $x = 0$ are compared for these seven different radii r in Fig. 13. Excellent agreement is observed. Figure 14 compares the u_x/U as a function of x/r at $y = 0$ for both the downstream and upstream regions for these seven different radii. Again, all seven cases compare very well even in the near wall region. This clearly demonstrates that the present boundary condition treatment has maintained geometric fidelity even with coarse grid resolutions.

It is noted that the interpolation for $\tilde{f}_{\bar{\alpha}}(\boldsymbol{x}_b, t)$ given by Eq. (17) is carried along the line in the direction of $\boldsymbol{e}_\alpha$. The results for flow over a cylinder are quite satisfactory. Other interpolation procedures can certainly be devised to use more information on neighboring lattices in the flow field. However, this will result in a lot more complications in the implementation. It is not clear if such an attempt will necessarily lead to further improvement over the present approach.

IV. CONCLUSION

In this work a second-order accurate boundary condition treatment for the lattice Boltzmann equation is proposed. A series of studies are conducted to systematically validate the accuracy and examine the robustness of the proposed boundary condition in steady and unsteady flows involving flat and curved walls. Compared with the existing method for treating boundary condition in the lattice Boltzmann method, the proposed treatment has the following advantages: (i) It can preserve the geometry of interest without truncating

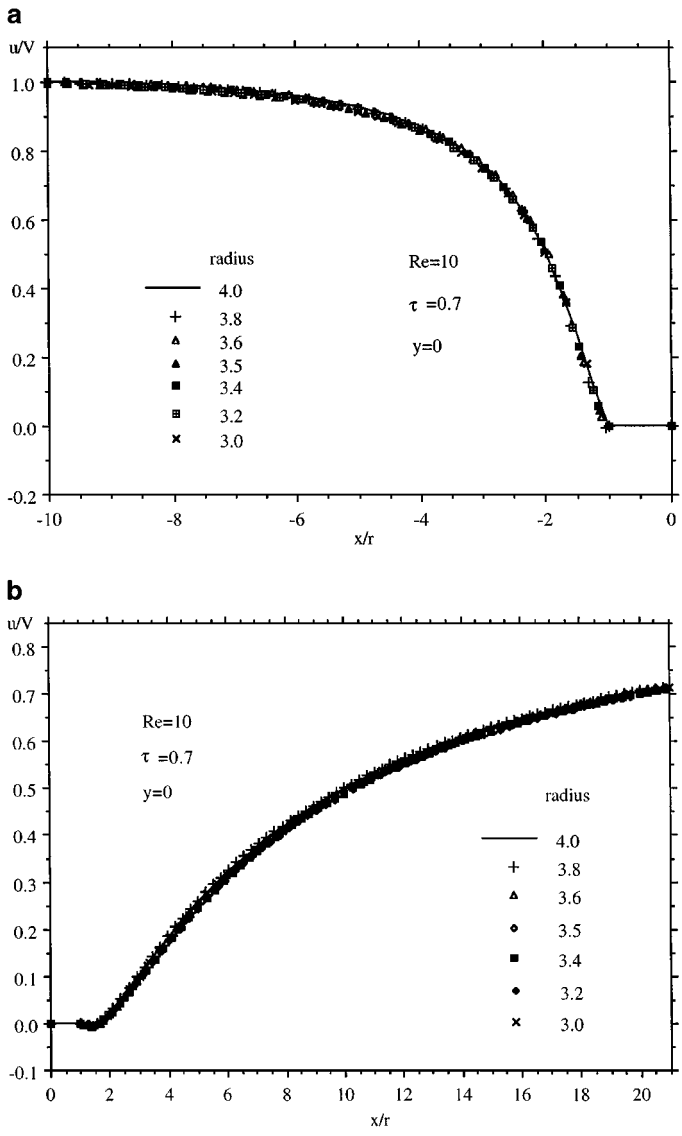

FIG. 14. Comparison of the centerline velocity for $r = 3.0$, 3.2, 3.4, 3.5, 3.6, 3.8, and 4.0 for $\mathrm{Re} = 10$ and $H/r = 20$. (a) Upstream region; (b) downstream region.

it into a series of stair steps. (ii) The boundary treatment generally results in solutions of second-order accuracy for the velocity field in space, and in time for some cases. (iii) Compared with the widely used bounce-back on the link scheme, the present treatment gives comparable or better results for the flow field under otherwise identical computational parameters.

ACKNOWLEDGMENTS

This work is supported by the NASA Langley Research Center. R. Mei also acknowledges partial support of the Alcoa Foundation, the Engineering Research Center (ERC) for Particle Science and Technology at the

University of Florida, the National Science Foundation (EEC-9402989), and Industrial partners of the ERC. W. Shyy acknowledges partial support of AFOSR and Eglin AFB. The authors are grateful to Dr. Filippova and Professor Hänel for helpful discussions.

REFERENCES

1. G. McNamara and G. Zanetti, Use of the Boltzmann equation to simulate lattice-gas automata, *Phys. Rev. Lett.* **61**, 2332 (1988).
2. F. Higuera, S. Succi, and R. Benzi, Lattice gas dynamics with enhanced collisions, *Europhys. Lett.* **9**, 345 (1989).
3. H. Chen, S. Chen, and W. H. Matthaeus, Recovery of the Navier–Stokes equations using a lattice-gas Boltzmann method, *Phys. Rev. A* **45**, R5339 (1992).
4. R. Benzi, S. Succi, and M. Vergassola, The lattice Boltzmann equation: Theory and applications, *Phys. Rep.* **222**, 145 (1992).
5. S. Chen and G. D. Doolen, Lattice Boltzmann method for fluid flows, *Ann. Rev. Fluid Mech.* **30**, 329 (1998).
6. R. Peyret and T. D. Taylor, *Computational Technique for Fluid Dynamics* (Springer-Verlag, New York, 1983), Vol. II.
7. C. A. J. Fletch, *Computational Techniques for Fluid Dynamics* (Springer-Verlag, New York, 1988), Vols. I, II.
8. W. Shyy, *Computational Modeling for Fluid Flow and Interfacial Transport*, corrected printing (Elsevier, Amsterdam, 1997).
9. P. L. Bhatnagar, E. P. Gross, and M. Krook, A model for collision processes in gases. I. Small amplitude processes in charged and neutral one-component system, *Phys. Rev. A* **94**, 511 (1954).
10. X. He and L.-S. Luo, A priori derivation of the lattice Boltzmann equation, *Phys. Rev. E* **55**, R6333 (1997).
11. X. He and L.-S. Luo, Theory of the lattice Boltzmann equation: From Boltzmann equation to lattice Boltzmann equation, *Phys. Rev. E* **56**, 6811 (1997).
12. T. Abe, Derivation of the lattice Boltzmann method by means of the discrete ordinate method for the Boltzmann equation, *J. Comput. Phys.* **131**, 241 (1997).
13. Y. H. Qian, D. d'Humières, and P. Lallemand, Lattice BGK models for Navier–Stokes equation, *Europhys. Lett.* **17**, 479 (1992).
14. U. Frisch, B. Hasslacher, and Y. Pomeau, Lattice-gas automata for the Navier–Stokes equation, *Phys. Rev. Lett.* **56**, 1505 (1986).
15. D. H. Rothman and S. Zaleski, *Lattice-Gas Cellular Automata: Simple Models of Complex Hydrodynamics* (Cambridge Univ. Press, New York, 1997).
16. D. P. Ziegler, Boundary conditions for lattice Boltzmann simulations, *J. Stat. Phys.* **71**, 1171 (1993).
17. I. Ginzbourg and P. M. Alder, Boundary flow condition analysis for the three-dimensional lattice Boltzmann model, *J. Phys. II France* **4**, 191 (1994).
18. X. He, Q. Zou, L.-S. Luo, and M. Dembo, Analytic solutions and analysis on non-slip boundary condition for the lattice Boltzmann BGK model, *J. Stat. Phys.* **87**, 115 (1997).
19. O. Behrend, Solid boundaries in particle suspension simulations via lattice Boltzmann method, *Phys. Rev. E* **52**, 1164 (1995).
20. L.-S. Luo, Analytic solutions of linearized lattice Boltzmann equation for simple flows, *J. Stat. Phys.* **88**, 913 (1997).
21. A. J. C. Ladd, Numerical simulation of particular suspensions via a discretized Boltzmann equation. Part 2. Numerical results, *J. Fluid Mech.* **271**, 311 (1994).
22. D. R. Noble, S. Chen, J. G. Georgiadis, and R. O. Buckius, A consistent hydrodynamic boundary condition for the lattice Boltzmann method, *Phys. Fluid* **7**, 203 (1995).
23. S. Chen, D. Martinez, and R. Mei, On boundary conditions in lattice Boltzmann method, *Phys. Fluids* **8**, 2527 (1996).

24. Q. Zou and X. He, On pressure and velocity boundary conditions for the lattice Boltzmann BGK model, *Phys. Fluids* **9**, 1591 (1997).
25. X. He, L.-S. Luo, and M. Dembo, Some progress in lattice Boltzmann method. Part I. Nonuniform mesh grids, *J. Comput. Phys.* **129**, 357 (1996).
26. X. He, L.-S. Luo, and M. Dembo, Some progress in lattice Boltzmann method: High Reynolds mesh grids, *Phys. A* **239**, 276 (1997).
27. X. He and G. Doolen, Lattice Boltzmann method on curvilinear coordinates system: Flow around a circular cylinder, *J. Comput. Phys.* **134**, 306 (1997).
28. R. Mei and W. Shyy, On the finite difference-based lattice Boltzmann method in curvilinear coordinates, *J. Comput. Phys.* **143**, 426 (1998).
29. I. Ginzbourg and D. d'Humières, Local second-order boundary methods for lattice Boltzmann models, *J. Stat. Phys.* **84**, 927 (1996).
30. O. Filippova and D. Hänel, Grid refinement for lattice-BGK models, *J. Comput. Phys.* **147**, 219 (1998).
31. X. He and L.-S. Luo, Lattice Boltzmann model for the incompressible Navier–Stokes equation, *J. Stat. Phys.* **88**, 927 (1997).
32. L.-S. Luo, Unified theory of the lattice Boltzmann models for non-ideal gases, *Phys. Rev. Lett.* **81**, 1618 (1998).
33. R. Mei, J. Xiong, and R. Tran-Son-Tay, Motion of a sphere oscillating at low Reynolds numbers in a visco-elastic-fluid-filled cylindrical tube, *J. Non-Newtonian Fluid Mech.* **66**, 169 (1996).